

# 3D finite element simulation for tool temperature distribution and chip formation during drilling of Ti6Al4V alloy

Zhaoju Zhu (✉ [zhuzhaoju0216@163.com](mailto:zhuzhaoju0216@163.com))

Shandong University

Zhu Yunqi

Sun Xinhui

Gao Chuhang

Lin Zhimao

He Bingwei

---

## Research Article

**Keywords:** Finite element model, Temperature distribution, Chip formation, Drilling, Ti6Al4V alloy

**Posted Date:** March 15th, 2022

**DOI:** <https://doi.org/10.21203/rs.3.rs-1430104/v1>

**License:**   This work is licensed under a Creative Commons Attribution 4.0 International License.

[Read Full License](#)

---

# **3D finite element simulation for tool temperature distribution and chip formation during drilling of Ti6Al4V alloy**

Zhaoju Zhu\*, Yunqi Zhu, Xinhui Sun, Chuhang Gao, Zhimao Lin, Bingwei He

School of Mechanical Engineering and Automation, Fuzhou University, Fujian, PR China

E-mail: [zhuzhaoju0216@163.com](mailto:zhuzhaoju0216@163.com)

**Abstract:** A comprehensive 3D finite element simulation study has been conducted to investigate the tool temperature distribution along cutting edge and chip formation during drilling of Ti6Al4V alloy by using commercial finite element software Abaqus/Explicit. The Johnson-Cook material constitutive model and material failure criterion were implemented across the formulations to achieve the tool temperature and chip formation in the drilling process. The effect of different mesh sizes on simulation results was also analyzed. To assess and verify the accuracy of the simulation model, the corresponding experiment studies were carried out by measuring the thrust force, tool temperature, and chip morphology. Compared results show that the predicted thrust force, temperature distribution, and chip morphology are in good agreement with those tested from experiments. According to the combination of both simulations and experiments, it can be not only found the whole varying pattern of the thrust force but also reveal that the temperature decreases from drill center to outer corner along the primary cutting edge. In addition, it can provide a more detailed and profound knowledge about chip formation. All these are assumed to be recommendations for the optimization of tool geometry and drilling processing.

**Keywords:** Finite element model, Temperature distribution, Chip formation, Drilling, Ti6Al4V alloy

## **1. Introduction**

Drilling as one of the most complex manufacturing processes covers a large

variety of applications in the automotive and aircraft manufacturing industries for structural assembly, which can account for more than 50% of all total machining processes [1-3]. The development of these manufacturing industries has increased the use of difficult-to-machine materials [4, 5]. Titanium alloys as typical difficult-to-machine materials are widely used in aerospace, biomedical, and automotive processing components owing to their excellent combination of high specific strength, high-temperature resistance, and corrosion resistance [6, 7]. However, due to their inherent properties, it is prone to generate high cutting force, high tool temperature, serious tool wear, and short drill life during the drilling process [5]. These characteristics lead to significant consumption of drilling tools and a significant increase in the cost of machining. Several researchers have used finite element simulation to simulate drilling operations, then designed and optimized tool structure parameters based on the simulation results to improve machining accuracy and surface quality. An accurate drilling model is critical in finite element simulation.

At present, lots of researches are primarily using simulation software such as Abaqus, Deform, and ThirdWaveSystems AdvantEdge to acquire thrust forces and temperatures [8-10]. ThirdWaveSystems AdvantEdge is a dedicated machining simulation software with a large material database and pre-defined simulation models, which is extremely easy to use. However, if the simulation is not conducted according to its pre-defined model, the simulation results may be inaccurate and report errors. Abaqus is a highly capable software for nonlinear analysis. Therefore, Abaqus/Explicit software was chosen for 3D finite element simulation for tool temperature distribution and chip formation during drilling of Ti6Al4V alloy in this paper.

Bonnet [11] proposed a multi-scale model based on a hybrid numerical/experimental approach to obtain local information and investigated the strain and temperature at different locations on the main cutting edge of the drill by using Abaqus. The results showed that the non-uniform temperature distribution was mainly due to the variation of cutting speed and rake angle along the main cutting edge and confirmed that most of the heat generated during the drilling process was discharged by the chips. Isbilir [12] used Abaqus to build a 3D drilling simulation model, taking

into account factors such as damage to the workpiece material, tool-workpiece contact properties, and process parameters. This model was also verified by the experimental thrust force, torque, and burr height. Girion [13] proposed a new numerical simulation method for calculating residual stresses in drilling based on Abaqus. They simulated the thermal effects generated by material removal through the process parameters and then derived the residual stresses using Lagrange's formula. Nan [10] achieved large deformation of the workpiece and chip formation during drilling in a finite element simulation. However, this model was conducted using a workpiece with the same inclination angle as the point angle of the drill, which can not fully reflect the real situation as a rectangular workpiece was drilled. Priest [14] carried out a comparative analysis of chip separation methods using Abaqus and Deform-3D software and found that the updated-Lagrangian method with dynamic re-mesh was more accurate. Yildiz [15] used Deform-3D to study the effect of tool coating and chip parameters on thrust forces and torque, and also analyzed the effect of thrust forces and torque on the stresses of the drill bit. Korkmaz [16] studied the J-C model parameters of AISI 430 material using Deform-3D and verified the validity of the J-C model parameters through experiments and simulations, confirming that the J-C model parameters can be applied to any machining simulation. Matsumura [17] used AdvantEdge to simulate a 2D cutting model instead of a 3D drilling model to predict thrust forces to improve simulation efficiency and save time. Lazoglu [18] investigated a new thermoelectric-based temperature measurement system-RTT and used Comsol finite element simulation to achieve tool temperature distribution prediction. Chatterjee [19] used Deform-3D to build a 3D drilling model based on the Lagrangian method for predicting thrust forces and drilling temperatures, but this model did not reflect the presence of chips during the drilling process. Lotif [8] used Deform-3D to build a three-dimensional drilling model to predict heat generated on the drilling face and tool flank wear, confirming that an increase in feed rate led to an increase in local temperature at the cutting edge. Fan [20] changed the structure of a double-cone drill to reduce the effect of chips on the drilling quality, showing that the effect of chips on the drilling process is not negligible.

Nowadays, during the drilling simulation process by using Abaqus/Explicit, most research was only concentrated on the mesh cells removing, which can not reflect the flowing chips. From the aforementioned studies, it can be understood that chips have a very important influence on thrust forces and drilling temperatures. This is because the chips can take away most of the cutting heat and reduce the tool temperature directly. In addition, the accumulated chips in the drilling hole can result in the thrust force increasing. Therefore, the tool temperature distribution and chip formation mechanism are worth to be understood. For this purpose, a 3D finite element simulation model based on Lagrange's formula for tool temperature distribution and chip formation during drilling of Ti6Al4V alloy was conducted in this paper, and the accuracy of this model was assessed and verified by corresponding experimental tests.

## **2. Modeling and analysis**

A 3D simulation model for titanium alloy drilling has been conducted by using the finite element package Abaqus/Explicit.

First, the geometric models of the workpiece and the tool are created, and the geometric models of the tool and the workpiece are given material parameters, constitutive parameters, and material failure criteria. Then the tool and the workpiece are assembled, the degrees of freedom of the tool and the workpiece are restricted, and machining parameters are applied to the tool so that the tool is feeding according to a pre-defined path.

### **2.1 Tool and workpiece model**

In this paper, the tool material is Cemented Carbide (WC-Co)-YG8, whose physical and mechanical properties are shown in [Table 1](#). A 3D model was constructed in Solidworks based on the physical model of the YG8 tool. To ensure the efficiency of the finite element simulation, the tool of the 3D model was split to reduce the mesh division, and only the drill part was used in this model for simulation, and [Fig. 1](#) shows the results of the model build. Only considering the influence of the process parameters of the tool on the drilling temperature distribution and drilling forces of the cutting edge,

without considering the wear and deformation of the tool, the tool is set as a rigid body in this model.

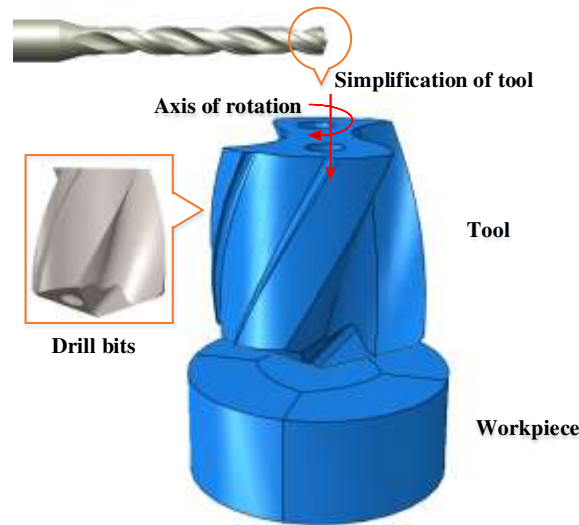


**Fig. 1** The cutting tool model

**Table 1**

Physical and mechanical properties of YG8 [21]

Density ( $\text{kg} \cdot \text{m}^{-3}$ )	Elastic modulus ( $\text{GPa}$ )	Poisson's ratio	Thermal conductivity ( $\text{W} \cdot \text{m}^{-1} \cdot \text{°C}^{-1}$ )	Specific heat ( $\text{J} \cdot \text{kg}^{-1} \cdot \text{°C}^{-1}$ )
14600	$6.4 \times 10^5$	0.22	75.4	220

The workpiece for the machining experiment is a Ti6Al4V rectangular plate with the chemical composition shown in Table 2. Since the analysis time in Abaqus is related to the number of meshes and the feed rate, to reduce the analysis time in Abaqus, a cylindrical workpiece with a thickness of 3 mm and a diameter of 6 mm is created in this model in Abaqus, and this workpiece model is used to equate the workpiece in the actual machining.

**Table 2**

Chemical compositions of Ti6Al4V [22]

Elements	Ti	Al	V	Fe	C	N	H	O
Wt%	Base	5.5-6.75	3.5-4.5	<0.25	<0.08	<0.05	<0.01	<0.2

## 2.2 Material parameters of the model

Material parameters significantly affect the outcome of finite element simulations. A material constitutive model symbolizes a mathematical representation of the

relationship between the flow stress and the temperature, strain, and strain rate of a material. The accuracy of the simulation results is directly related to the material constitutive model. At the moment, researchers have worked on several material constitutive models, including Johnson-Cook, Steinberg-Guinan, Zerilli-Armstrong, and Follansbee-Kocks. In the field of metal cutting simulation, the Johnson-Cook constitutive model is preferred as the workpiece material's constitutive model for simulation, as it reflects the physical and mechanical properties of metal materials at large strains, high strain rates, and high temperatures [23]. Johnson-constitutive Cook's model mathematical expression as the following Eq. (1).

$$\sigma = (A + B\varepsilon^n) [1 + C \ln \frac{\dot{\varepsilon}}{\dot{\varepsilon}_0}] [1 - (\frac{T - T_r}{T_m - T_r})^m] \quad (1)$$

Where  $\sigma$  is the equivalent stress,  $\varepsilon$  is the equivalent plastic strain,  $\dot{\varepsilon}$  is the equivalent plastic strain rate,  $\dot{\varepsilon}_0$  is the reference strain rate. The parameters  $T$ ,  $T_m$ ,  $T_r$  are the current cutting temperature, respectively. The physical and mechanical properties of Ti6Al4V are listed in Table 3. The Johnson-Cook parameter A, B, n, C, m for Ti6Al4V are defined in Table 4.

**Table 3**

Physical and mechanical properties of Ti6Al4V [22]

Density ( $\text{kg} \cdot \text{m}^{-3}$ )	Elastic modulus ( $\text{GPa}$ )	Poisson's ratio	Thermal conductivity ( $\text{W} \cdot \text{m}^{-1} \cdot \text{K}^{-1}$ )	Specific heat ( $\text{J} \cdot \text{kg}^{-1} \cdot \text{K}^{-1}$ )	Thermal expansion coefficient ( $\text{K}^{-1}$ )	Melting temperature ( $\text{K}$ )
4430	109 (50°C)	0.34	6.8 (20°C)	611 (20°C)	9.0E-6	1605°C
	91 (250°C)		7.4 (100°C)	624 (100°C)		
	75 (450°C)		9.8 (300°C)	674 (300°C)		
			11.8 (500°C)	703 (500°C)		

**Table 4**

Johnson-Cook constitutive model parameters of Ti6Al4V [24]

Initial yield stress $A(\text{MPa})$	Hardening modulus $B(\text{MPa})$	Strain hardening coefficient $n$	Strain rate dependency coefficient $C$	Thermal softening coefficient $m$
782	492	0.28	0.028	1

## 2.3 Material failure criteria

The metal material undergoes elastic deformation and plastic deformation during the drilling process and then damage begins to occur, which continues until the material

is completely fractured. The stress-strain curve during material deformation is shown in Fig. 2. The curve  $O-A$  is the elastic deformation stage of the material and the slope  $(d\sigma/d\varepsilon)$  is the modulus of elasticity of the material  $E$ .  $\sigma_s$  indicates the maximum stress to which the material is subjected during the elastic deformation phase. The curve  $A-B$  shows the uniform plastic deformation phase of the material, where strain hardening of the material plays a major role. At point  $B$ ,  $(d\sigma/d\varepsilon)$  is equal to zero, is the critical point of material initial damage, the slope of the curve after the formation of damage  $(d\sigma/d\varepsilon)$  is less than zero, the material enters the non-uniform plastic deformation phase, the phase of damage evolution. When material damage accumulates and reaches the fracture criterion, there is a complete loss of material stiffness at which failure occurs.

To better reflect the chip separation state. In this paper, the Johnson-Cook shear failure model [25] is chosen, and the equation is as (2)

$$w = \sum \frac{\Delta \bar{\varepsilon}}{\bar{\varepsilon}_{JC}} \quad (2)$$

$D$  is the state variable associated with the equivalent plastic strain of the material.  $\Delta \bar{\varepsilon}$  is the equivalent plastic strain increment.  $\bar{\varepsilon}_{JC}$  is the plastic strain at failure at the current strain rate, temperature, and stress state.  $w$  is accumulated at the end of each incremental step of the analysis, and when  $w$  equals 1, the material begins to fail. The JC damage model for the failure plastic strain  $\bar{\varepsilon}_{JC}$  is shown in Eq. (3)

$$\bar{\varepsilon}_{JC} = (d_1 + d_2 \exp d_3 \frac{P}{\sigma}) (1 + d_4 \ln \frac{\dot{\varepsilon}}{\dot{\varepsilon}_0}) [1 - d_5 (\frac{T-T_r}{T_m-T_r})^m] \quad (3)$$

$P$  is the hydrostatic stress, which is the average of the three principal stresses.  $d_1 - d_5$  is the failure parameter of the material, which denotes the initial failure strain, the exponential factor, the stress triaxiality factor, the strain rate factor, and the temperature factor, whose values are shown in Table 5. Eq. (3) shows that the failure plastic strain  $\bar{\varepsilon}_{JC}$  is determined by the combination of the stress triaxiality  $\frac{P}{\sigma}$ , the equivalent effect rate of change, the deformation temperature, and the material failure parameters.

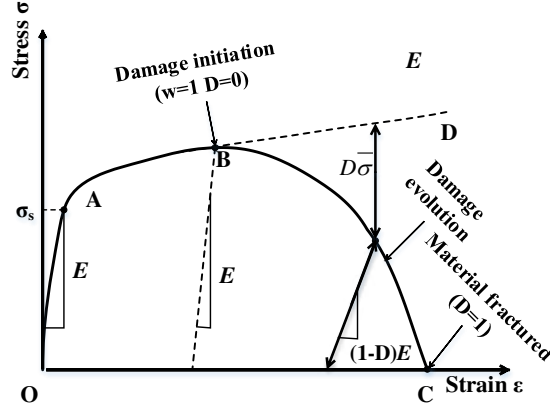


Fig. 2 Typical uniaxial Stress-strain response of the material failure process [26]

Table 5

Parameters of Johnson-Cook failure model for Ti6Al4V [27]

$d_1$	$d_2$	$d_3$	$d_4$	$d_5$
-0.09	0.25	-0.5	0.014	3.87

## 2.4 Chip separation

During drilling operations, the relative motion between the tool and the workpiece causes friction in the contact area. An accurate cutting friction model is critical in metal cutting simulations, where friction is an important component in generating drilling forces and drilling heat. Currently, the most popularly used model in metal cutting is the modified Coulomb model [28]. According to the theory proposed by Zorev [29], as shown in Eq. (4), the friction between the chip and the front tool face consists of two parts, namely the sticking region and the sliding region[30, 31]. As shown in Fig. 3, the sticking region is the area on the rake face near the tooltip. This area generates sticking friction due to high drilling heat and the squeezing effect of chips on the rake face, and the heat is higher than that of the sliding region. The sliding region is the area on the rake face away from the tool tip. This area gradually reduces the sliding friction caused by the squeezing effect on the rake face as the chips are discharged along the front tool face, the cutting heat is quickly dissipated and the temperature is lower compared to the bonded area [32]. The friction coefficient between the tool and the workpiece in this model is 0.4.

$$\begin{cases} \tau = \mu\sigma & \tau < \bar{\tau}_{max} \quad (\text{sticking region}) \\ \tau = \bar{\tau}_{max} & \tau > \bar{\tau}_{max} \quad (\text{sliding region}) \end{cases} \quad (4)$$

Where,  $\tau$  is the friction stress.  $\mu$  is the friction coefficient.  $\sigma$  is the normal stress.

$\bar{\tau}_{max}$  is the shear flow stress.

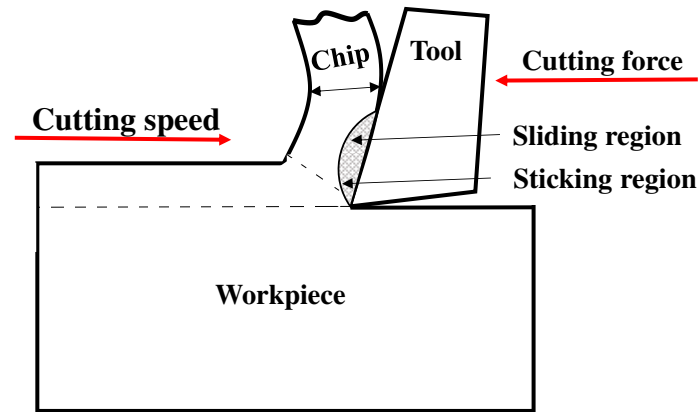
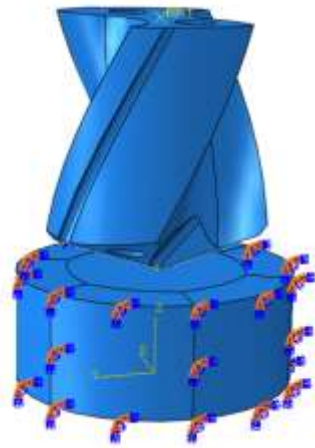


**Fig. 3** Model of chip-to-tool friction

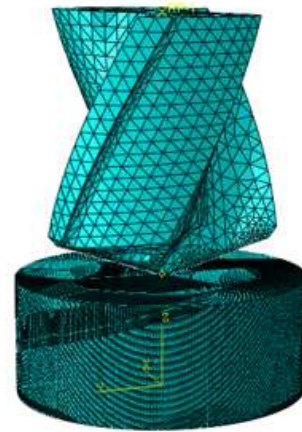
## 2.5 meshing and boundary conditions

In actual machining production, the fixture clamps the workpiece to constrain the six degrees of freedom of the workpiece. In the simulation, the side of the workpiece is fully constrained to simulate the actual machining situation where the workpiece is constrained. A reference point is set on the tool, which is given a forward feeding motion and a rotational motion around the axis. As shown in Fig. 4.a. In this model, the drill mesh type is set to C3D4T (four-node thermally coupled tetrahedral cell). In Fig. 5.a, the number of meshes at the chisel edge and main cutting edge is increased during the tool mesh division. This has the advantage of improving the accuracy of the simulation and avoiding errors during the simulation caused by tool intrusion into the workpiece. Fig. 5.b shows that the workpiece mesh type is set to C3D8RT (eight-node thermally coupled hexahedral cell). R stands for reduced integration, which is used to improve simulation efficiency. In general, to improve simulation efficiency and accuracy, the workpiece is divided into machining region and non-machining region, with a dense mesh in the machining region and a relatively sparse mesh in the non-machining region. However, in this model, to further improve the efficiency of the simulation, the non-machined area of the workpiece is cut and the useless mesh is removed to obtain the minimum non-machined area. Finally, the tool model was divided into 32476 meshes and the workpiece was divided into 927870 meshes, after which the tool and the workpiece were assembled, and the assembly results are shown

in Fig. 4.b.



(a) boundary conditions



(b) mesh assembly drawing

**Fig. 4** Assembly body



(a) Tool mesh distribution



(b) Workpiece mesh distribution

**Fig. 5** Mesh distribution

### 3. Result and discussion

The drilling experiments were carried out on a DAEWOO ACE-V500 vertical machining cent. Fig. 6 shows the experimental setup and the signal acquisition system. The drilling parameters and tool information for the experiments are shown in Table 6. Before the experiment, a workpiece of 220 mm in length, 100 mm in width, and 3 mm in thickness was fixed on a dynamometer (Kistler 9273) with a fixture to collect the thrust force of the tool during the drilling process, and the experiment was performed by dry cutting.

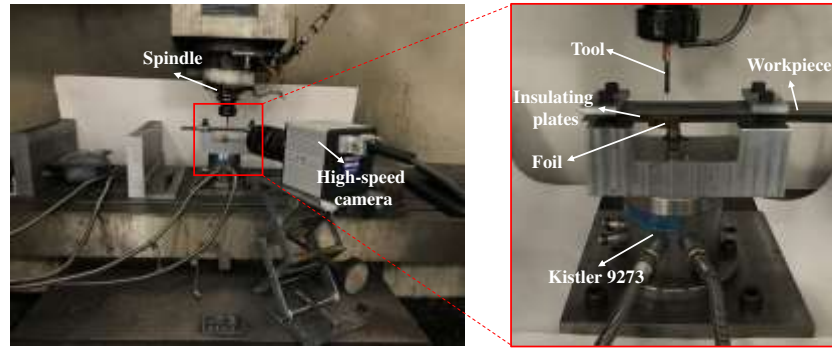


**Fig. 6** The drilling experimental platform

**Table 6**

Tool information and drilling parameters

Tool materials	Cemented Carbide (WC-Co)-YG8	
Tool information	Diameter /mm	3.6
	Number of Teeth	2
	point angle	140°
	Spiral angle	35°
	Blade length /mm	20
	Coating	Uncoated
Drilling parameters	Cutting speed /m·min <sup>-1</sup>	26/40/55
	Feed rate /mm·r <sup>-1</sup>	0.05/0.13/0.2

### 3.1 Effect of mesh size on thrust forces

Mesh division is an essential part of finite element simulation. The mesh size and style are the external factors that influence the accuracy of drilling simulation. The change of mesh size influences the deformation and failure behavior of the workpiece material, which in turn influences the thrust force magnitude during the drilling process. In this paper, the simulations will be carried out using five groups of models with the same cutting parameters but with different mesh sizes (20 $\mu$ m, 30 $\mu$ m, 40 $\mu$ m, 50 $\mu$ m, 60 $\mu$ m), comparing the thrust forces of the five simulations and selecting an accurate and effective mesh size for the subsequent simulations. To improve the efficiency of the simulation in this section, the simulation was carried out under the cutting parameters of feed rate 0.2mm/r and cutting speed 55m/min. The values of drilling forces for different sizes of meshes with constant cutting parameters are shown in Fig. 7.

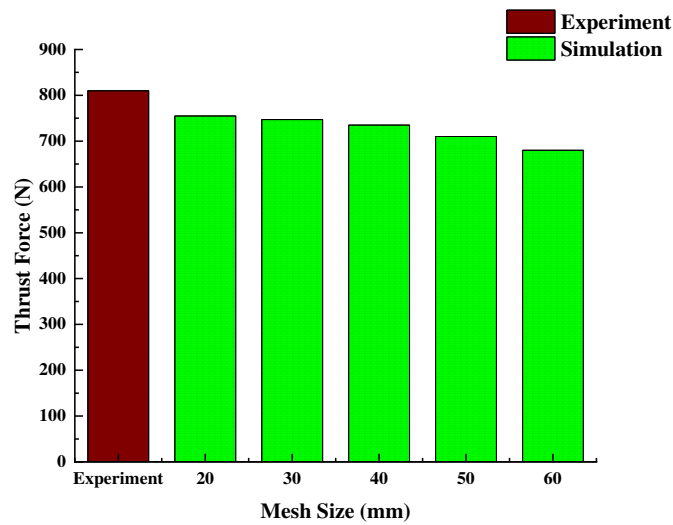


**Fig. 7** Comparison of simulated and experimental thrust forces for different mesh sizes

From [Fig. 7](#), it can be seen that the smaller the mesh size is, the more accurate the simulation results are. When the mesh size is less than 40 $\mu$ m, the simulation accuracy is not significantly improved, but the simulation time required increases exponentially. In this model, the mesh size of 40 $\mu$ m is used for the subsequent simulation taking into account the time cost and simulation efficiency.

## 3.2 Experimental verification of the simulation model

### 3.2.1 Thrust force

Thrust force being the key physical in the material removal process, it is a critical indicator to evaluate the mechanical energy consumption required for the interaction between the tool and the workpiece. The magnitude of thrust force has a great influence on cutting temperature and machining quality. [Fig. 8](#) shows the experimental and simulated thrust force change curve with drilling depth in titanium alloy drilling at a cutting speed of 26 m/min and a feed rate of 0.05 mm/r. This curve can be divided into three segments.

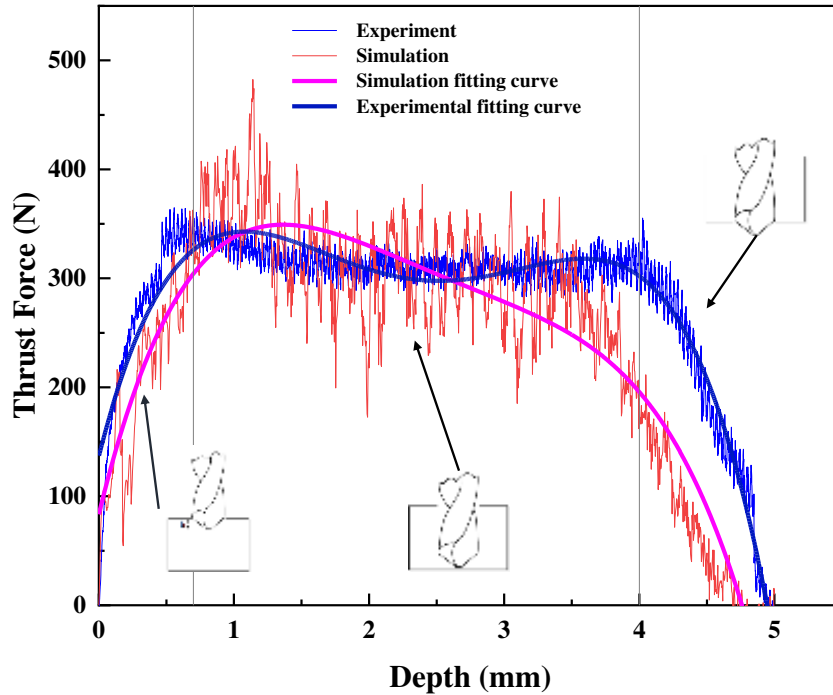


**Fig. 8** Experimental and simulated thrust force variation characteristics

**Fig. 9** represents the change rule of tool thrust force with cutting speed and feed rate measured in the Ti6Al4V machining experiment. This rule is also reflected in the present simulation model (**Fig. 10a**). It can be seen from the graph that the thrust force increases with the increase of the feed rate at the cutting speed of 55m/min. When the feed rate increases from 0.05mm/r to 0.2mm/r, the thrust force of the tool increases from 295N to 810N, while the thrust force of the simulation model increases from 340N to 735N. This is primarily due to the fact that a larger feed rate represents a larger material removal rate, which means a larger amount of drilling per unit time, and therefore results in a larger increase in thrust force. It can be seen from **Fig. 9** and **Fig. 10b** that the influence of cutting speed on the thrust force is minor. At the feed rate of 0.13mm/r, the cutting speed increases from 25m/min to 55m/min and the thrust force decreases slightly. This is due to the fact that as the cutting speed increases, the friction between the tool and the workpiece becomes larger, which leads to an increase in the heat generated by friction and serious thermal softening of materials and causes a slight decrease in the cutting force.

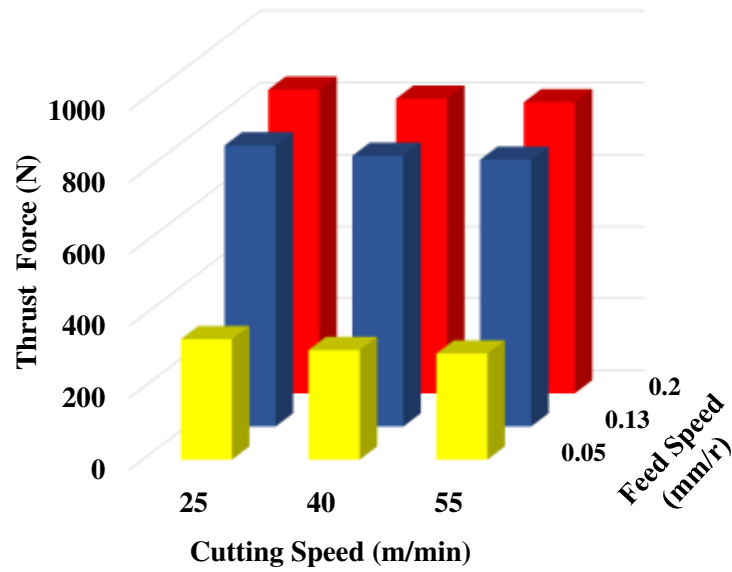


Fig. 9 Variation of thrust forces with cutting parameters

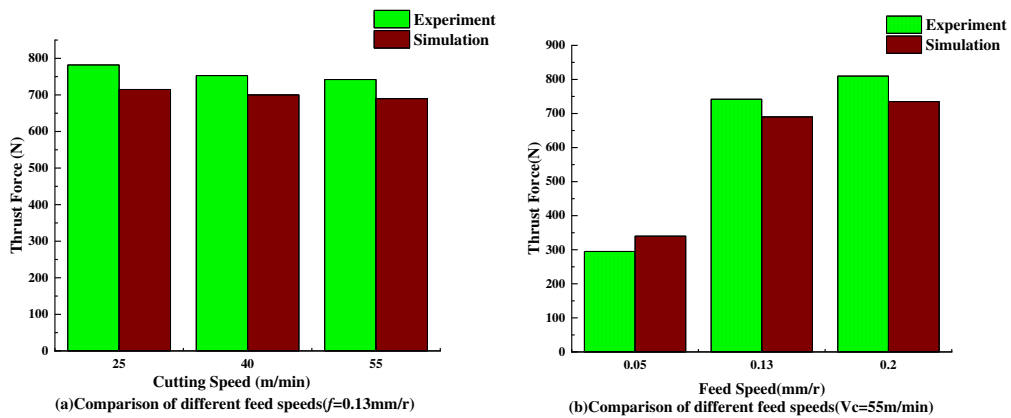


Fig. 10 Comparison between simulation and experiment

### 3.2.2 Temperature

During the material removal process, most of the mechanical energy is converted into thermal energy, which is transferred to the chip, workpiece, and tool in different proportions. During the drilling process, the heat generated on the main cutting edge is uneven due to the different cutting speeds, tool front angles, and cutting edge inclination of the various parts of the main cutting edge. In practice, chips can carry a lot of heat that is difficult to remove from the hole, causing the hole temperature to rise. Because of the complexity of the drilling scenario, measuring drilling temperatures is more difficult than measuring cutting temperatures, so an accurate drilling simulation model is important.

In this paper, the Tool-Foil thermoelectric method will be used to verify the

temperature distribution characteristics on the main cutting edge of the tool in the simulation model. The theoretical support for this method is based on the Seebeck effect. The Seebeck effect is the electromotive force (EMF) that develops across two points of an electrically conducting material when there is a temperature difference between them. The EMF is called the Seebeck EMF (or thermoelectric EMF).

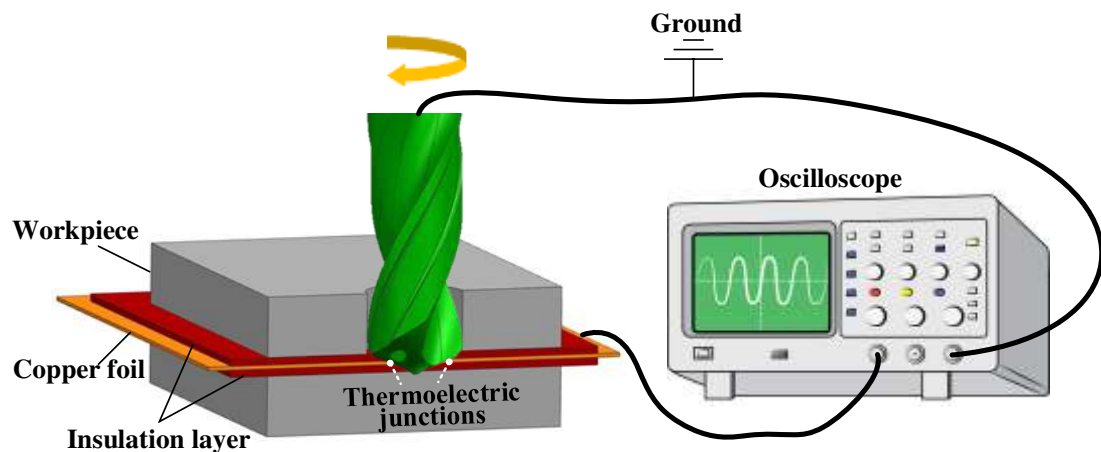


Fig. 11 Schematic diagram of the drilling temperature measurement principle [3]

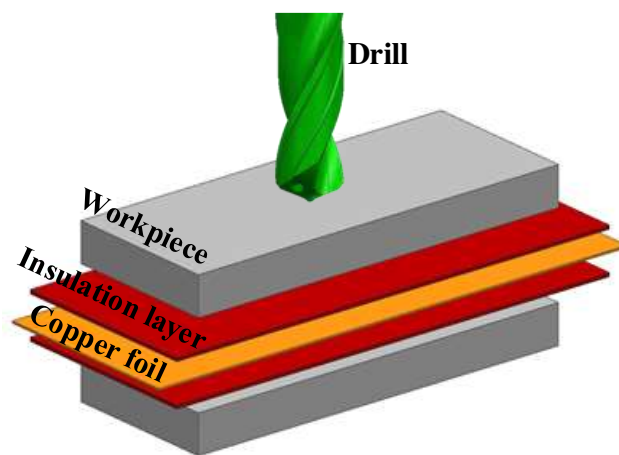


Fig. 12 Exploded view [3]

A schematic diagram of the principle of measuring the temperature distribution on the main cutting edge using the Tool-foil thermoelectric system is shown in Fig. 11. A copper foil of 0.05 mm thickness is sandwiched between the upper and lower workpieces and the workpieces are insulated from the copper foil by insulating plates of 0.25 mm thickness respectively, forming a thermoelectric pair with the tool (Fig.12). The end of the copper foil away from the working area is used as the cold end of the thermoelectric and is connected to one pole of the data collector. The tool is connected

to the other pole of the data collector by means of a brush, ensuring that the circuit consisting of the tool and the workpiece is broken before the tool touches the copper foil. During the drilling process, when the drill tip starts to contact the copper foil, the thermal contact point between the cutting edge and the foil forms one end of a thermoelectric, and there is a certain temperature difference with the cold end, generating an EMF which flows in a circuit consisting of the tool - copper foil - data collector and connecting wires, completing the EMF acquisition. This EMF to the temperature of that contact point on the cutting edge. As the drilling continues, the thermal contact point moves along the main cutting edge from the tip to the outer edge, thus generating a continuous EMF signal indicating the distribution of the EMF on the main cutting edge during the drilling process. The EMF is only generated and collected in the circuit when the drill tip is in contact with the copper foil. When the drill tip has partially passed all the way through the foil, a path is formed between the cutter body and the foil, making the interference signal increase. There are two points to note: firstly, to reduce the influence of noise and other interference during the measurement process, ground the circuit; secondly, to reduce the measurement error and ensure the accuracy of the measurement results, the part of the tool connected to the brush is wrapped in the same material as the brush to avoid the generation of secondary EMF.

In order to determine the relationship between the measured EMF and temperature, a calibration test of the EMF and temperature was carried out with the aid of a standard type thermoelectric. As shown in [Fig. 13](#), a standard OMEGA thermoelectric (type 5TC-TT-K-40-36) was placed infinitely close to a contact point consisting of a tool and copper foil, and a heater was used to heat both the contact point position and the thermoelectric to ensure that the temperature measured by the thermoelectric was the same as the temperature at the contact point.

A Japanese YOKOGAWA (DL750) data acquisition system was used to simultaneously acquire the temperature signal measured by the thermoelectric and the EMF signal generated at the contact point to obtain the calibration curve between temperature and EMF, as shown in [Fig. 14](#), and after fitting a quadratic polynomial to obtain the function between temperature  $T$  and EMF  $U$ .

$$T = -27.34U^2 + 242.45U + 39.28 \quad (5)$$

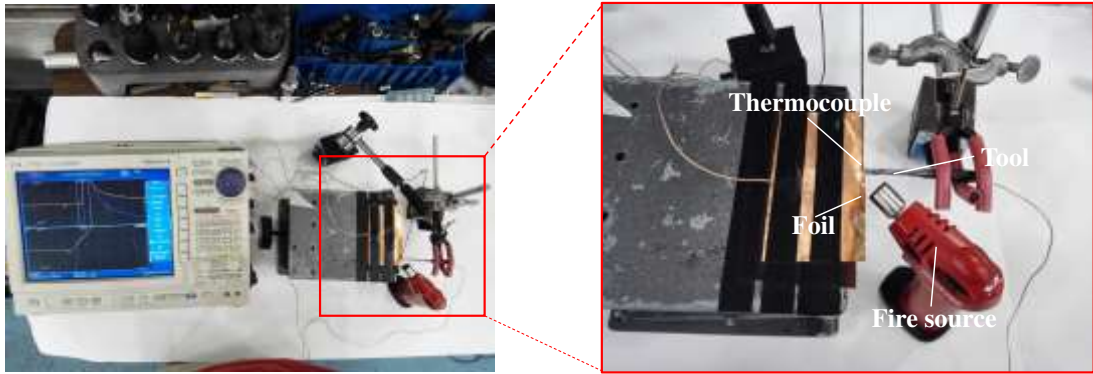


Fig. 13 Temperature and thermoelectric calibration devices

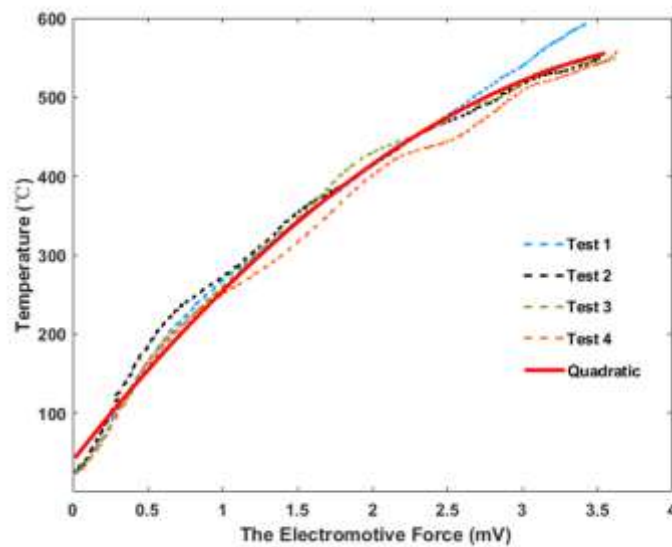
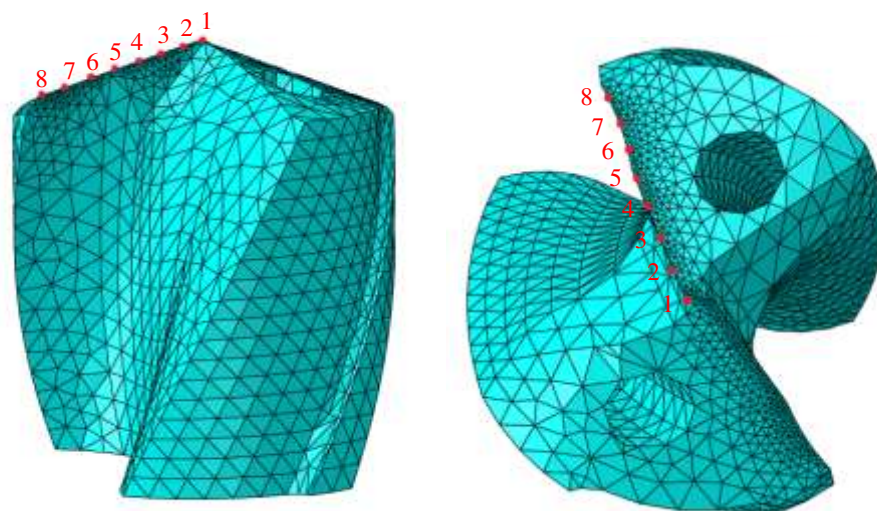


Fig. 14 Temperature and EMF calibration curve

As shown in Fig. 15, eight cells are divided on the main cutting edge of the tool in the simulation model. These eight cells are set as a set, and these eight cells are bound to the temperature in the history variable. The temperature distribution on the main cutting edge can be obtained by exporting the temperature of these eight cells during the post-processing of the simulation. Under the cutting parameters of cutting speed 55m/min and feed rate 0.2mm/r, the temperature nephogram of this simulation model is shown in Fig. 16. It can be seen that the drilling temperature tends to gradually decrease from the drill center to the outer edge of the cutting edge, which indicates that the drill center temperature is higher than the temperature of the outer edge of the cutting edge. This is due to the unique structural characteristics of the main cutting edge

of the drill. It is because the rake angle of the tool, the inclination angle and the cutting speed change gradually along the main cutting edge from the center to the outer edge. Near the drilling center position, the rake angle of the tool is small with a negative rake angle, which makes cutting difficult, and the cutting speed of the tool is almost zero. However, there is still feed movement, which causes a serious wedge splitting phenomenon and generates a larger cutting force, while the rake angle of the outer edge of the cutting edge is larger, the cutting edge is relatively sharper and generates less cutting force. In addition, the cutting speed is too low near the center part, which leads to the heat generated can not being discharged in time, and as the cutting continues, the heat in the cutting area gradually accumulates to cause the temperature near the drill center position is higher than the temperature of the outer edge of the cutting edge.

The curve of the experimentally measured main cutting edge temperature of the drills fitted to the main cutting edge temperature of the drill finite element simulation drill is shown in Fig. 17. The deviation between simulation and experiment can be expressed by the mean square deviation *RMS* (Root Mean Square) and the error percentage *P*, as shown by Eq. (6) (7).



**Fig. 15** Distribution of units along the main cutting edge

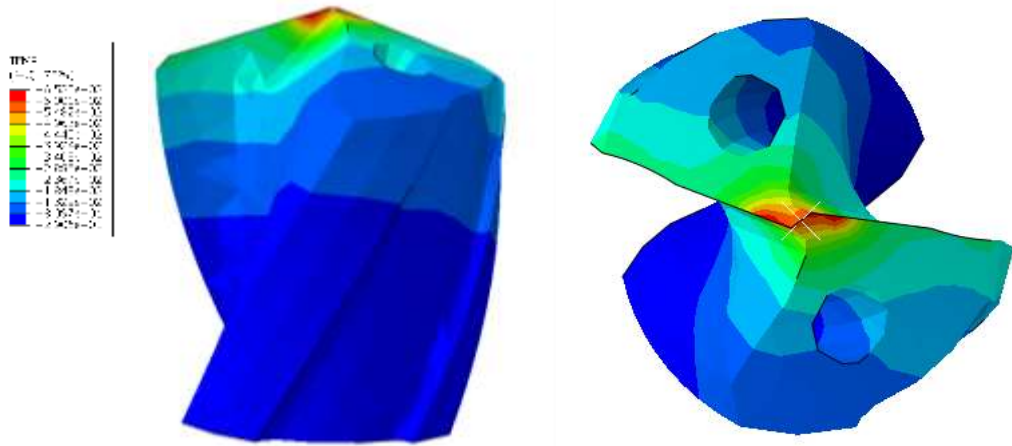


Fig. 16 Temperature nephogram

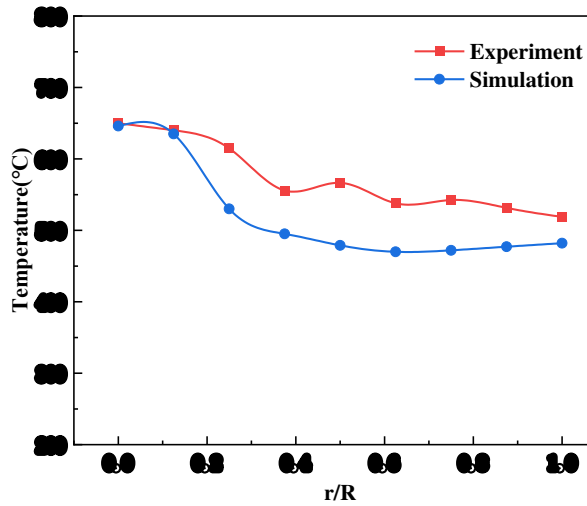


Fig. 17 Experimental and simulation temperatures

$$RMS = \sqrt{\frac{1}{N} \sum_{i=1}^N (T_{exp}^{i} - T_{est}^{i})^2} \quad (6)$$

$$P = \frac{RMS}{T_{max}} \quad (7)$$

$T_{exp}$  is the measured temperature,  $T_{est}$  is the simulated temperature,  $N$  is the number of measured temperatures and  $T_{max}$  is the maximum value of the measured temperature. The  $RMS$  and  $P$  of the curve in Fig. 18 are calculated to be 52.355 and 7.99% respectively, the smaller  $RMS$  and  $P$  indicate that the experimental results are in better coincidence with the simulation results, which verifies the accuracy of the simulation results.

### 3.3 Chip morphology

In actual machining, the generation of thrust force is related to a variety of factors,

in which the frictional resistance generated by the chip curl also affects the thrust force. At present, most drilling simulation models of Abaqus do not reflect the chip, so that the composition of the thrust force will lack the part of frictional resistance due to chip curling, which will cause the simulation results to be less accurate.

In order to better understand the chip formation process in the machining of drilling, a three-dimensional chip formation schematic was established (Fig. 18). In the drilling process, the drills first come into contact with the workpiece material and friction. Under the combined effect of the extrusion of the drills and frictional heat, the shear force exceeds the yield limit of the workpiece. The surface layer is plastically deformed, the lattice is dislocated, and slip to occurs, resulting in chips (Fig. 18a). Because of the different cutting speeds on the main cutting edge, the cutting speed near the drill point is much slower than the cutting speed near the outer edge of the drill, which means that the cutting has a speed difference on the main cutting edge, causing the chips to curl laterally (Fig. 18b).

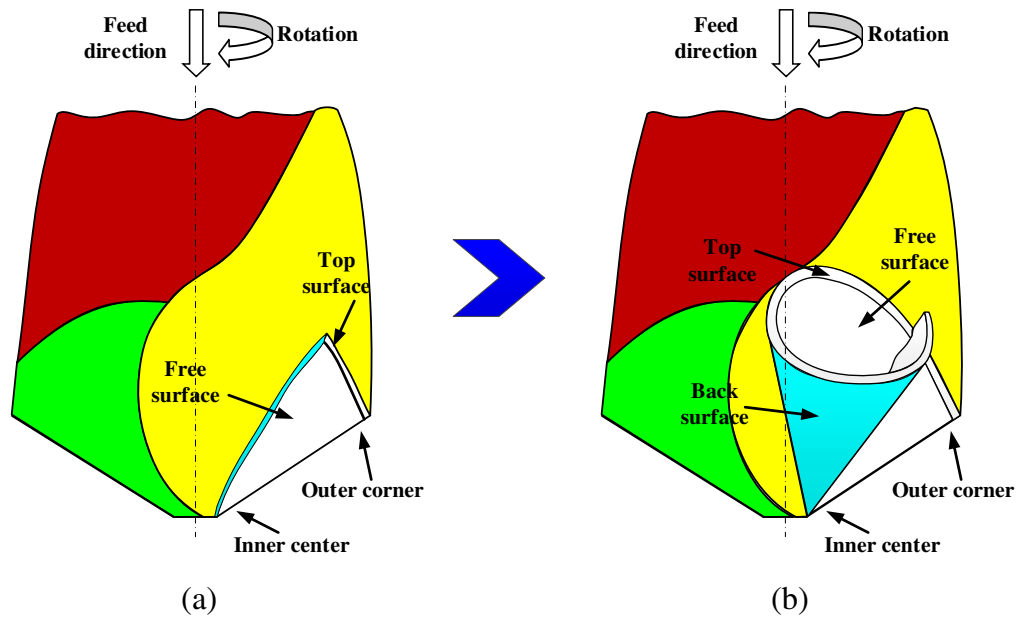
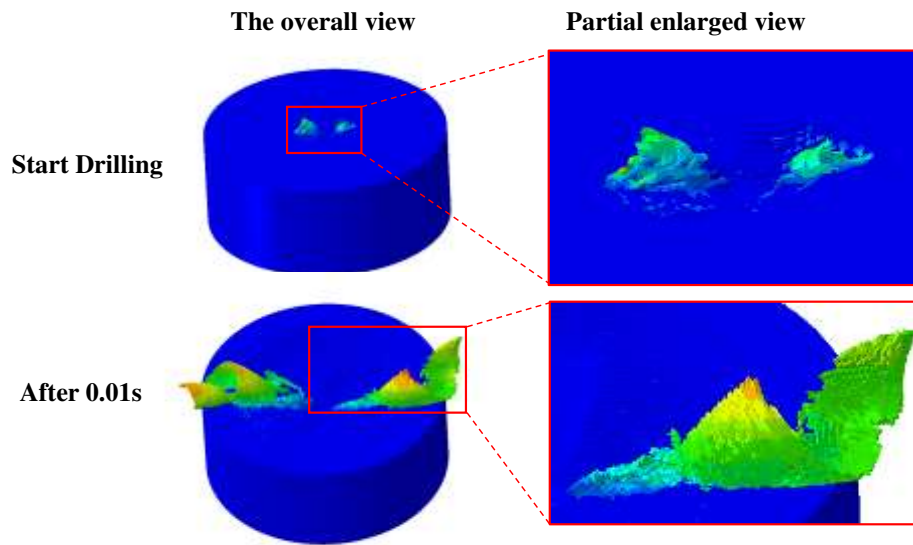
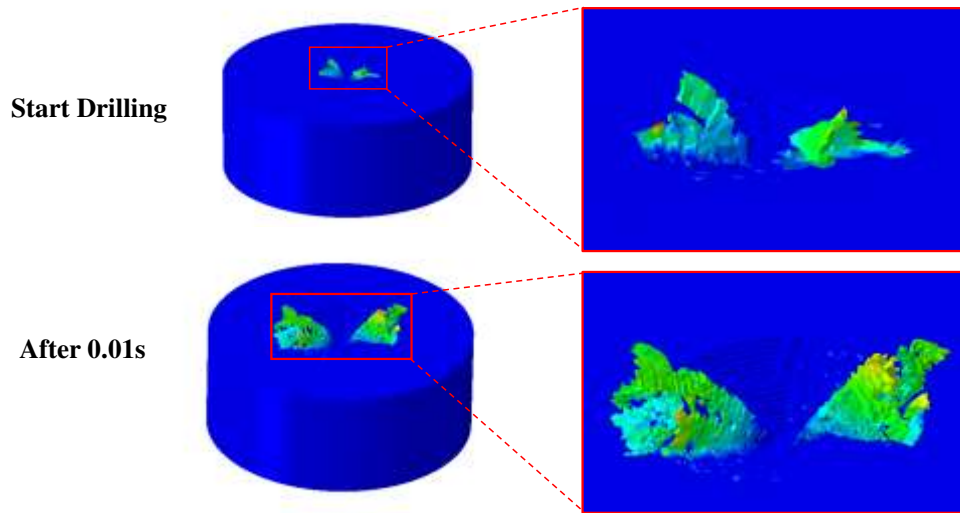


**Fig. 18** 3D schematic of chip forming, (a) chip formation, (b) chip curl. [33]

In this paper, the simulation model established has a better representation of the chips in the drilling process. The cutting speed of 55m/min and the feed rate of 0.2 mm/r is used for the finite element simulation of drilling chips, and the simulation results are compared with the experiments. The results are shown in Fig. 19.



(a) chip morphology of 40 $\mu$ m



(b) chip morphology of 60 $\mu$ m

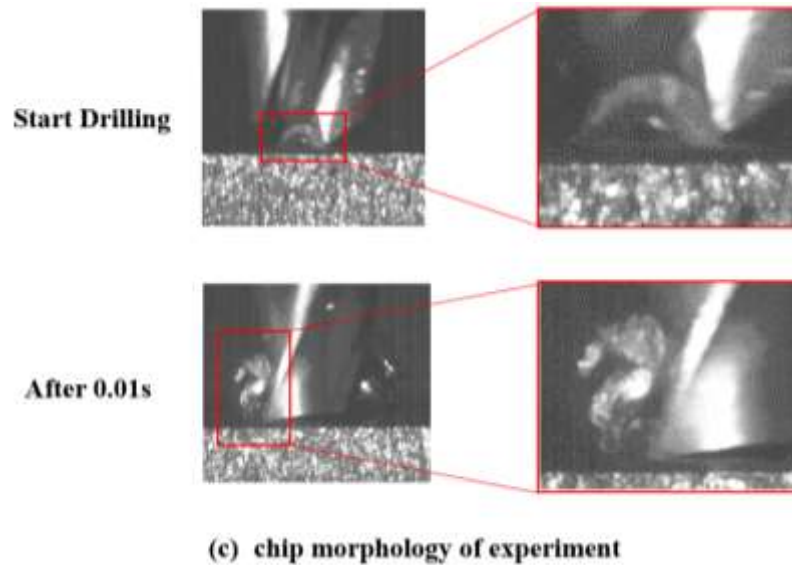


**Fig. 19** Simulated chip representation

Fig. 19(c) shows the chip shape at the beginning of chip generation and after 0.01s of machining using a high-speed camera (cutting speed 55m/min, feed rate 0.2mm/r). In Fig. 12(a) (b), the simulation results are shown for the workpiece with a mesh size of 40  $\mu\text{m}$  and 60  $\mu\text{m}$  respectively. The right side of the picture shows the partial enlargement which shows that the chip produced by the mesh size of 60 $\mu\text{m}$  already tends to fracture. This is because the mesh size is large compared to the depth of cut per revolution and the cell mesh cannot properly simulate the material flow around the cutting edge. In contrast, the smaller mesh size of Fig. 19(a) allows the material flow around the cutting edge to be simulated, and chip generation can be better predicted. It can be concluded that the smaller the mesh size, the more realistic the prediction of the chip morphology. However, there is a consequent increase in computational cost. The curled chips simulated by this model are more consistent with the experimentally generated curled chips, and this can effectively reflect the frictional resistance generated by the chips, which makes the simulation results of the thrust force more accurate.

## 4 Conclusions

In this paper, a three-dimensional drilling finite element model was established with Abaqus/Explicit simulation software to study the change law of axial force, main

cutting edge temperature distribution and chip generation with the change of mesh size and cutting parameters when the model was drilling Ti6Al4V. And the following conclusions were drawn.

1. The mesh division affects the accuracy of the simulation. A smaller mesh size means higher simulation accuracy and longer computation time. When the grid size is smaller than a value, the simulation accuracy does not change significantly, but the computation time will continue to increase. In this paper, the simulation accuracy does not change significantly when the grid size is less than  $40\mu\text{m}$ , so the grid size of  $40\mu\text{m}$  is selected as the critical size for the subsequent simulation.
2. This simulation model's accurate prediction of the thrust force reveals that the thrust force increases with the increase of the feed rate and decreased with the increase of the cutting speed, which is in accordance with the objective laws.
3. This simulation model predicts the temperature distribution on the main cutting edge and reveals that the temperature on the main cutting edge decreases gradually from the drill center to the outer edge during drilling.
4. This simulation model predicts chip formation and reveals the effect of different mesh sizes on chip formation. The smaller the mesh size, the better the representation of chip flow in the simulation, but the computational time for the same simulation increases.

**Author contribution** Zhaoju Zhu and Binwei He worked on conceptualization, methodology, formal analysis, and preparation of the original draft with input from all authors. Yunqi Zhu and Xinhui Sun developed the computational modal, design optimization, and conducted the experiments. Chuhang Gao and Maozhi Lin worked on data collection, processing, and segmentation. Zhaoju Zhu supervised the project.

**Funding** This work is financially supported by Natural and science foundation of Fujian Province under grant numbers 2021J01560 and Education and scientific research foundation for young teachers in Fujian Province under grant numbers JAT190006.

**Availability of data and material** The raw/processed data required to reproduce these

findings cannot be shared at this time as the data also forms part of an ongoing study.

**Code availability** Not applicable.

## **Declarations**

**Ethics approval** Not applicable.

**Consent to participate** Not applicable.

**Consent to publication** Not applicable

**Conflicts of interest** The authors have no conflicts of interest to declare that are relevant to the content of this article.

## **References**

- [1] P.A. Rey, J. LeDref, J. Senatore, Y Landon (2016) Modelling of cutting forces in orbital drilling of titanium alloy Ti-6Al-4V, *International Journal of Machine Tools and Manufacture*, 106 75-88. <https://doi.org/10.1016/j.ijmachtools.2016.04.006>
- [2] R. Han, J. Wu (2010) Finite Element Simulation of Drilling Based on Third Wave Systems AdvantEdge, *Key Engineering Materials - KEY ENG MAT*, 431-432 229-232. <https://doi.org/10.4028/www.scientific.net/KEM.431-432.229>
- [3] Z. Zhu, B. He, J. Chen (2020) Evaluation of tool temperature distribution in MQL drilling of aluminum 2024-T351, *Journal of Manufacturing Processes*, 56 757-765. <https://doi.org/10.1016/j.jmapro.2020.05.029>
- [4] Z. Zhu, S. Sui, J. Sun, J. Li, Y. Li (2017) Investigation on performance characteristics in drilling of Ti6Al4V alloy, *The International Journal of Advanced Manufacturing Technology*, 93 651-660. <https://doi.org/10.1007/s00170-017-0508-6>
- [5] Z. Zhu, K. Guo, J. Sun, J. Li, Y. Liu, Y. Zheng, L. Chen (2018) Evaluation of novel tool geometries in dry drilling aluminium 2024-T351/titanium Ti6Al4V stack, *Journal of Materials Processing Technology*, 259 270-281. <https://doi.org/10.1016/j.jmatprotec.2018.04.044>
- [6] M. Balaji, K. Venkata Rao, N. Mohan Rao, B.S.N. Murthy (2018) Optimization of drilling parameters for drilling of TI-6Al-4V based on surface roughness, flank wear and drill vibration, *Measurement*, 114 332-339. <https://doi.org/10.1016/j.measurement.2017.09.051>
- [7] Z. Zhu, J. Sun, J. Li, P. Huang (2016) Investigation on the influence of tool wear upon chip morphology in end milling titanium alloy Ti6Al4V, *The International Journal of Advanced Manufacturing Technology*, 83 1477-1485. <https://doi.org/10.1007/s00170-015-7690-1>
- [8] M. Lotfi, S. Amini, I.Y. Al-Awady (2018) 3D numerical analysis of drilling process: heat, wear, and built-up edge, *Advances in Manufacturing*, 6 204-214. <https://doi.org/10.1007/s40436-018-0223-z>
- [9] F. Hu, L. Xie, J. Xiang, U. Umer, X. Nan (2018) Finite element modelling study on small-hole peck drilling of SiCp/Al composites, *The International Journal of Advanced Manufacturing Technology*, 96 3719-3728. <https://doi.org/10.1007/s00170-018-1730-6>
- [10] X. Nan, L. Xie, W. Zhao (2015) On the application of 3D finite element modeling for small-diameter

- hole drilling of AISI 1045 steel, *The International Journal of Advanced Manufacturing Technology*, 84 1927-1939. <https://doi.org/10.1007/s00170-015-7782-y>
- [11] C. Bonnet, T. Pottier, Y. Landon (2021) Development of a multi-scale and coupled cutting model for the drilling of Ti-6Al-4V, *CIRP Journal of Manufacturing Science and Technology*, 35 526-540. <https://doi.org/10.1016/j.cirpj.2021.08.007>
- [12] O. Isbilir, E (2011) Ghassemieh, Finite Element Analysis of Drilling of Titanium Alloy, *Procedia Engineering*, 10 1877-1882. <https://doi.org/10.1016/j.proeng.2011.04.312>
- [13] M. Girinon, F. Valiorgue, H. Karaouni, É. Feulvarch (2018) 3D numerical simulation of drilling residual stresses, *Comptes Rendus Mécanique*, 346 701-711. <https://doi.org/10.1016/j.crme.2018.06.003>
- [14] J. Priest, H. Ghadbeigi, S. Avar-Soberanis, S. Gerardis (2021) 3D finite element modelling of drilling: The effect of modelling method, *CIRP Journal of Manufacturing Science and Technology*, 35 158-168. <https://doi.org/10.1016/j.cirpj.2021.06.001>
- [15] A. Yıldız, A. Kurt, S. Yağmur (2020) Finite element simulation of drilling operation and theoretical analysis of drill stresses with the deform-3D, *Simulation Modelling Practice and Theory*, 104. <https://doi.org/10.1016/j.simpat.2020.102153>
- [16] M.E. Korkmaz (2020) Verification of Johnson-Cook parameters of ferritic stainless steel by drilling process: experimental and finite element simulations, *Journal of Materials Research and Technology*, 9 6322-6330. <https://doi.org/10.1016/j.jmrt.2020.03.045>
- [17] T. Matsumura, S. Tamura (2015) Cutting Simulation of Titanium Alloy Drilling with Energy Analysis and FEM, *Procedia CIRP*, 31 252-257. <https://doi.org/10.1016/j.procir.2015.03.045>
- [18] I. Lazoglu, G. Poulachon, C. Ramirez, M. Akmal, B. Marcon, F. Rossi, J.C. Outeiro, M. Krebs (2017) Thermal analysis in Ti-6Al-4V drilling, *CIRP Annals*, 66 105-108. <https://doi.org/10.1016/j.cirp.2017.04.020>
- [19] S. Chatterjee, S.S. Mahapatra, K. Abhishek (2016) Simulation and optimization of machining parameters in drilling of titanium alloys, *Simulation Modelling Practice and Theory*, 62 31-48. <https://doi.org/10.1016/j.simpat.2015.12.004>
- [20] L. Fan, D. Wang (2021) Study on delamination inhibition and chip breakage mechanism in drilling metal laminated materials with double cone drill, *Journal of Manufacturing Processes*, 64 81-94. <https://doi.org/10.1016/j.jmapro.2021.01.014>
- [21] Z. Hao, J. Li, Y. Fan, F. Ji (2019) Study on constitutive model and deformation mechanism in high speed cutting Inconel718, *Archives of Civil and Mechanical Engineering*, 19 439-452. <https://doi.org/10.1016/j.acme.2018.11.009>
- [22] B. Wang, Z. Liu (2016) Evaluation on fracture locus of serrated chip generation with stress triaxiality in high speed machining of Ti6Al4V, *Materials & Design*, 98 68-78. <https://doi.org/10.1016/j.matdes.2016.03.012>
- [23] G.R. Johnson (1983) A constitutive model and data for materials subjected to large strains, high strain rates, and high temperatures, *Proc. 7th Inf. Sympto. Ballistics*, 541-547.
- [24] D. Umbrello (2008) Finite element simulation of conventional and high speed machining of Ti6Al4V alloy, *Journal of Materials Processing Technology*, 196 79-87. <https://doi.org/10.1016/j.jmatprotec.2007.05.007>
- [25] I. ABAQUS, ABAQUS analysis user's manual: version 6-5, Rising Sun Mills, Providence, 2 (2004).
- [26] Y.C. Zhang, T. Mabrouki, D. Nelias, Y.D. Gong (2011) Chip formation in orthogonal cutting considering interface limiting shear stress and damage evolution based on fracture energy approach,

- Finite Elements in Analysis and Design, 47850-863. <https://doi.org/10.1016/j.finel.2011.02.016>
- [27] Y. Zhang, T. Mabrouki, D. Nelias, Y. Gong (2011) FE-model for Titanium alloy (Ti-6Al-4V) cutting based on the identification of limiting shear stress at tool-chip interface, *International Journal of Material Forming*, 4 11-23. <https://doi.org/10.1007/s12289-010-0986-7>
- [28] T.H.C. Childs (2006) Friction modelling in metal cutting, *Wear*, 260 310-318. <https://doi.org/https://doi.org/10.1016/j.wear.2005.01.052>
- [29] N. Zorev (1963) Inter-relationship between shear processes occurring along tool face and shear plane in metal cutting, *International research in production engineering*, 49 143-152.
- [30] G. Barrow, W. Graham, T. Kurimoto, Y.F. Leong (1982) Determination of rake face stress distribution in orthogonal machining, *International Journal of Machine Tool Design and Research*, 22 75-85. [https://doi.org/10.1016/0020-7357\(82\)90022-1](https://doi.org/10.1016/0020-7357(82)90022-1)
- [31] L.C. Lee, X.D. Liu, K.Y. Lam (1995) Determination of stress distribution on the tool rake face using a composite tool, *International Journal of Machine Tools and Manufacture*, 35 373-382. [https://doi.org/10.1016/0890-6955\(94\)E0020-J](https://doi.org/10.1016/0890-6955(94)E0020-J)
- [32] S. Kato, K. Yamaguchi, M. Yamada (1972) Stress Distribution at the Interface Between Tool and Chip in Machining, *Journal of Engineering for Industry*, 94 683. <https://doi.org/10.1115/1.3428229>
- [33] Z. Zhu, K. Guo, J. Sun, J. Li, Y. Liu, L. Chen, Y. Zheng (2018) Evolution of 3D chip morphology and phase transformation in dry drilling Ti6Al4V alloys, *Journal of Manufacturing Processes*, 34 531-539. <https://doi.org/10.1016/j.jmapro.2018.07.001>